Knollenberg *et al.*
Progress in Earth and Planetary Science (2025) 12:53
https://doi.org/10.1186/s40645-025-00717-3

Progress in Earth and Planetary Science

RESEARCH ARTICLE Open Access

The miniRAD instrument for the MMX IDEFIX rover

J. Knollenberg[1*], M. Grott[1], M. Hamm[1,2], A. Ihring[3], R. Ziese[1,2] and J. Biele[4]

Abstract

The miniRAD radiometer is one of the payloads of the Idefix rover on the MMX mission to Phobos. It is a multispectral instrument which measures the infrared radiative flux in six wavelength channels between 4.7 and 100 µm using single-element thermopile detectors. MiniRAD is equipped with optical filters, one centered at 5.5 µm, three narrow bandpass filters at 8.3 µm, 8.9 µm, and 9.5 µm and two longpass filters with cut-ons at 14–15 µm. One of the longpass filters made from boron nitride (BN) is especially optimized for very low flux, being sensitive in the very long wavelength region even beyond 50 µm. The main measurement objective of the miniRAD instrument is the determination of Phobos' surface brightness temperature during nighttime, from which the thermal inertia of the surface can be derived. Secondary objectives are to provide constraints on the slope of the emissivity in the thermal infrared, the location of the Christiansen feature, and the surface roughness of Phobos. MiniRAD has been calibrated radiometrically under relevant environmental conditions using a cavity blackbody over the full expected range of object temperatures from 100 to 330 K. The predicted uncertainty of the brightness temperature is < 1 K at dayside temperatures > 270 K for all channels, while the BN filter uncertainty is < 5 K at the lowest calibration temperature of 100 K.

Keywords Phobos, Mars Moon eXploration MMX, Rover, Idefix, MiniRAD, Radiometer, Thermal properties, Composition

*Correspondence:
J. Knollenberg
Joerg.Knollenberg@dlr.de
[1] German Aerospace Center, DLR, 12489 Berlin, Germany
[2] FU Berlin, 12249 Berlin, Germany
[3] Leibniz-IPHT, 07745 Jena, Germany
[4] German Aerospace Center, DLR, 51147 Cologne, Germany

Springer Open

© The Author(s) 2025. **Open Access** This article is licensed under a Creative Commons Attribution 4.0 International License, which permits use, sharing, adaptation, distribution and reproduction in any medium or format, as long as you give appropriate credit to the original author(s) and the source, provide a link to the Creative Commons licence, and indicate if changes were made. The images or other third party material in this article are included in the article's Creative Commons licence, unless indicated otherwise in a credit line to the material. If material is not included in the article's Creative Commons licence and your intended use is not permitted by statutory regulation or exceeds the permitted use, you will need to obtain permission directly from the copyright holder. To view a copy of this licence, visit http://creativecommons.org/licenses/by/4.0/.

1 Introduction

The Martian moons exploration, MMX, is JAXA's sample return mission targeting the two Martian moons Phobos and Deimos and is scheduled to launch in 2026 to return samples to Earth in 2031 (Nakamura et al. 2021; Kuramoto et al. 2022; Kawakatsu et al. 2023). The main scientific goal of the mission is to determine the origin of Phobos and Deimos and to investigate the evolution of the Martian moons. MMX will study the Martian system for 3 years and perform close-up observations of Phobos, while carrying out multiple flyby's of Deimos. Finally, the mission will collect samples from Phobos before returning to Earth.

The MMX Rover Idefix (Michel et al. 2022; Ulamec et al. 2023) is one of the MMX payloads and will investigate Phobos in-situ using a suite of scientific instruments comprised of a pair of stereo navigation cameras, another two cameras mounted underneath the rover to study the wheel–regolith interaction, a Raman spectrometer to study the mineralogical composition of Phobos' surface material, and the miniRAD radiometer to study the material's thermophysical and mineralogical properties. Idefix will bridge the scale gap between remote observations performed by the MMX spacecraft and the analysis of samples returned to Earth by providing measurements at the decimeter scale. Further, due to its locomotion capabilities, Idefix will be able to investigate the heterogeneity of surface properties along its traverse. By performing local measurements, the Idefix rover will in addition act as a surface scout and assist in selecting an appropriate and safe sampling site for the main spacecraft.

Current knowledge of the thermophysical and mineralogical properties of Phobos' regolith is rather limited, and spatially resolved measurements are particularly sparse (Smith et al. 2018). Current best estimates of surface thermal inertia are generally low and in the 20–85 J m^{-2} K^{-1} $s^{-1/2}$ range (Lunine et al. 1982; Ksanfomality et al. 1989; Kuehrt et al. 1992; Smith et al. 2018; Bandfield et al. 2018), thus being similar but slightly larger than disk averaged estimates for the Moon (Hayne et al. 2017). Regolith is assumed to be fine grained with average particle diameters in the few millimeter range (Gundlach and Blum 2013) and there are some indications for layering (Bandfield et al. 2018). Spectroscopic investigations indicate that the regolith may be basaltic in composition (Glotch et al. 2018).

The miniRAD instrument is a small lightweight spot radiometer on-board the Idefix rover dedicated to measure the thermal infrared emission from Phobos' surface in six wavelength channels between 5 and 100 µm. From these observations, miniRAD will determine the surface brightness temperature within the instrument's field of view. The instrument has strong heritage from the Rosetta MUPUS thermal mapper (Spohn et al. 2007, 2015), the MASCOT radiometer (Grott et al. 2017, 2019a, b), and the InSight radiometer (Spohn et al. 2018; Müller et al. 2020) using thermopile sensors for measuring the infrared flux (Kessler 2005). Each sensor has a field of view of 45° and will observe a spot at a distance of 25–150 cm in front of the rover. In this paper, we will discuss the miniRAD scientific objectives and describe the instrument design, calibration, and expected measurement performance.

2 Science objectives

The miniRAD instrument will investigate the thermophysical properties of Phobos' regolith and boulders and determine the variability of these properties along the rover's traverse. Using thermophysical models (e.g., Hamm et al. 2018), the miniRAD measurements will enable the determination of surface thermal inertia (Hamm et al. 2020), from which regolith porosity can be estimated if supplemental information from, e.g., camera images is available (Ogawa et al. 2019; Grott et al. 2020). Further, boulder porosity can be estimated based on thermal inertia measurements if heat capacity is assumed to be known (Grott el al. 2019a; b; Biele et al. 2022).

Using the emissivity in selected passbands (Hamm et al. 2022) derived from miniRAD data, the location of a spectral feature known as the Christiansen feature can be determined. The location of this emissivity maximum is diagnostic for rock forming minerals (and rock type), and the method of identifying mineralogy from emissivity estimates in three spectral bands has been pioneered by the Diviner team, who mapped the Moon on global scales (Cooper et al. 2002; Greenhagen et al. 2010; Lucey et al. 2021). Thus, miniRAD will allow for a first-order characterization of surface mineralogy on decimeter scales.

Measurements in the thermal infrared are sensitive to the presence of surficial dust layers (Biele et al. 2019; Hamm et al. 2023), and the shape of the diurnal temperature curve can be significantly affected by dust layer thicknesses of the order of 0.01 thermal skin depths (Biele et al. 2019), shifting the phase lag between maximum illumination and maximum temperature as well as strongly affecting the amplitude of the diurnal temperature curve. Skin depths on Phobos are expected to be close to 5 mm for regolith and of the order of a few centimeters for typical boulders, and consequently dust layers of 50 µm and 500 µm should be detectable, respectively.

Surface roughness strongly affects thermal emission on airless bodies (Kuehrt et al. 1992; Davidsson et al. 2014) and we will use a roughness model (Giese and Kuehrt 1990; Kuehrt et al. 1992; Lagerros 1996) to estimate surface roughness parameters. Roughness can significantly enhance the emitted flux at large solar zenith angles and

this effect is most pronounced at shorter wavelength (see, e.g., Michel et al. 2022). miniRAD employs a dedicated short wavelength channel to improve the constraints on the surface roughness model parameters and take the modified emission into account when deriving thermophysical parameters.

Finally, surface temperature variations can contribute to the disruption of surface rocks and thus contribute to the formation of regolith. This process is known as thermal fatigue (Molaro and Byrne 2012; Delbo et al. 2014; Molaro et al. 2017; Ruesch et al. 2022) and its efficiency is known to be insolation and latitude dependent (Hamm et al. 2019). miniRAD will contribute to studying the importance of thermal fatigue on Phobos by determining surface temperatures for full diurnal cycles at the different locations investigated.

A summary of the miniRAD science and measurement objectives is given in the science traceability matrix shown in Table 1, where the mission science goals, mission science objectives, miniRAD measurement objectives, and respective miniRAD measurements are given for the subset of MMX objectives miniRAD will contribute to. The miniRAD investigation focusses on surface composition, the characterization of physical properties, and surface alteration processes, and the table specifies which of the six miniRAD channels will be used to address a particular objective. It should be noted that measurements 1.1.1 and 1.1.2 (Table 1) in the spectral band passes around 8.3, 8.9, and 9.5 μm require only a short-term measurement of surface emission, while all other objectives associated with the determination of surface roughness, dust covers, diurnal temperature amplitudes, and surface thermophysical properties ideally rely on measurements of full diurnal temperature cycles.

3 Instrument design

3.1 Overview

miniRAD comprises three main parts, a sensor head (SH), a calibration target (CT), and an electronics box. The sensor head itself is made of three main parts, the SH body housing the infrared sensors, the SH flexprint cable making the electrical connection between the SH and the E-Box, and the SH mounting bracket adapting the SH body in the right orientation to the rover. The calibration target is an aerial blackbody mounted to the front shutter of the rover in such a way that it covers the miniRAD FOV when the front shutter is in closed position. The miniRAD electronics (EL) consists of a Rigid-flex assembly of two PCB's housed inside the electronics box which is itself located in the thermally controlled structural and electrical module (SEM) of the Idefix rover.

The miniRAD SH is mounted on the side panel of the rover outside the SEM such that it looks down to the surface with an angle of 35° with respect to horizontal, and slightly rotated around the vertical axis of the rover by about 15° (Fig. 1) to observe an approximately elliptical measurement spot in front of the rover. Figure 2 illustrates the measurement geometry assuming a flat terrain. The measurement spot of miniRAD lies nearly completely within the field-of-view of the rover's stereo navigation camera NAVCAM, except for a small part close to the rover This will allow the use of digital terrain models generated from NAVCAM images taken simultaneously with miniRAD measurements in the analysis of miniRAD data.

An overview of miniRAD engineering budget data and the most important performance characteristics is summarized in Table 2.

3.2 Mechanical design

The miniRAD sensor head consists of three parts, the SH body with radiation shield, the SH flexprint, and the mounting bracket. The SH body itself is composed of five main parts, a cylindrical block made from aluminum with the necessary cavities to accommodate six thermopile IR sensors and five temperature sensors of type Pt-100, an aluminum backplate with another integrated Pt-100 which closes the SH body to the rear side, a PCB to route the electrical signals from the different sensors to a nano-D connector, a reflective baffle for straylight suppression fixed by five M1.6 screws to the front face, and a cylindrical radiation shield (Fig. 3). All outer surfaces of the SH body are gold-coated to minimize the radiation losses to the environment. All aluminum parts of the SH body are machined using the alloy EN AW-6082.

A custom Kapton foil heater is glued around the SH cylindrical body with the thermally conductive and low outgassing silicone glue SCV-2499 from NuSil. The same glue is also used to fix the Pt-100 and IR sensors to the structure of the SH body. To further reduce radiation losses a low emissivity aluminum foil (outer layer of MLI) is applied on the outside surface of the Kapton foil heater. Four stainless steel standoffs are screwed into the SH body and act as an internal mechanical interface to the mounting bracket. Each stand-off is composed of two shorter stainless steel standoffs with a PEEK sleeve in the center for thermally isolating the radiation shield from the SH body. This design is driven by the requirement for thermal isolation of the SH while maintaining structural strength to withstand the mechanical loads during launch.

The mounting bracket main objectives are to provide the accommodation of the SH to the rover in such a way

Table 1 miniRAD Science Traceability Matrix: Science traceability matrix showing the overarching MMX science goals as well as the subset of those science objectives to which miniRAD directly or indirectly contributes by measuring net radiometric fluxes in the different passbands. Adapted from Michel et al. (2022)

Science objective	Measurement objective	Measurement
Science Goal 1: Origin of Phobos		
1.1 Determine the surface composition and formation conditions	1.1.1 Constrain surface mineralogy	Determine the location of the Christiansen Feature by radiometric surface brightness measurements at wavelengths of 8.2, 8.9, and 9.5 µm
	1.1.2 Constrain surface mineralogy	Determine the spectral slope in the IR wavelength range by radiometric surface brightness measurements at wavelengths of 4.7, 8.2, 8.9, and 9.5 µm
	1.1.3 Determine surface roughness	Radiometric surface brightness determination at 4.7, 8.2, 8.9, and 9.5 µm and the broadband channels as a function of solar incidence and phase angles
	1.1.4 Determine dust cover thickness/layering	Radiometric surface brightness determination in the broadband channels as a function of time
	1.1.5 Determine diurnal temperature amplitude/thermal fatigue	Radiometric surface brightness determination in the broadband channels as a function of time
Science Goal 2: Surface evolution and processes		
2.1 Characterization of physical properties and dynamics of regolith	2.1.1 Determine surface thermal inertia	Measure surface brightness temperature in the broadband channels
	2.1.2 Determine thermal conductivity	Measure surface brightness temperature in the broadband channels
	2.1.3 Determine porosity	Measure surface brightness temperature in the broadband channels
2.2 Surface alteration	2.2.1 Determine diurnal temperature amplitude/thermal fatigue	Radiometric surface brightness determination in the broadband channels as a function of time

that the field-of-view (FOV) of the miniRAD sensors overlaps with the FOV of the navigation camera on Phobos' surface, and to decouple the SH body thermally from the rover chassis. To achieve these goals, the bracket is manufactured from PEEK HP3 in 3D printing technology and has a rather complex geometry composed of different thin struts which interface on one side with the four standoffs of the SH body, and on the other side with the carbon composite rover side panel. The bracket design is a compromise between the requirement of low thermal conduction on one hand, and the requirements on stiffness (SH eigenfrequency ~ 230 Hz) and sufficient mechanical strength to withstand the mechanical launch loads on the other hand.

A flexible printed wiring board is used to connect the SH to the miniRAD E-Box Rigid-flex interface PCB. The flexprint is equipped on both sides with 37-pin nano-D flex connectors. Strain relief on the SH side is achieved using a clamp which is integrated into the SH bracket, while dedicated clamping parts attached to the nano-D connector provide the strain relief on the I/F PCB side.

The electronics box is composed of two similar half-shells made from Al-6082 which are connected together by four M3 screws. The box houses the miniRAD electronics, a Rigid-flex PCB design composed of two PCB's for the equipment of electrical components and a long Rigid-flex tail terminated by an I/F PCB. This terminal PCB is equipped with a 37-pin nano-D receptacle providing the electrical connection of the electronics to the SH flex cable. A single micro-D 21 Pin connector on the side wall of the E-Box provides the electrical interface (both power and data) to the rover power unit (PCDU) and onboard computer (OBC).

The calibration target is an approximately elliptical Al-MIC-6 plate with a pyramidal microstructure coated by Acktar™ fractal black. A Pt-100 temperature sensor and a custom Kapton foil heater are glued to the backside of the CT to enable temperature control. The CT plate is mounted by five M2 screws to a thermally isolating support structure made from PEEK which is itself fixed to the front shutter of the Idefix rover (Fig. 4).

3.3 Thermal design

The three miniRAD subunits, such as E-Box, sensor head, and calibration target, employ different concepts for their thermal control system (TCS) which shall guarantee that the subunits are working within their specified design temperature limits for all nonoperational or operational use cases. While the E-Box is collectively controlled together with other rover units inside the SEM

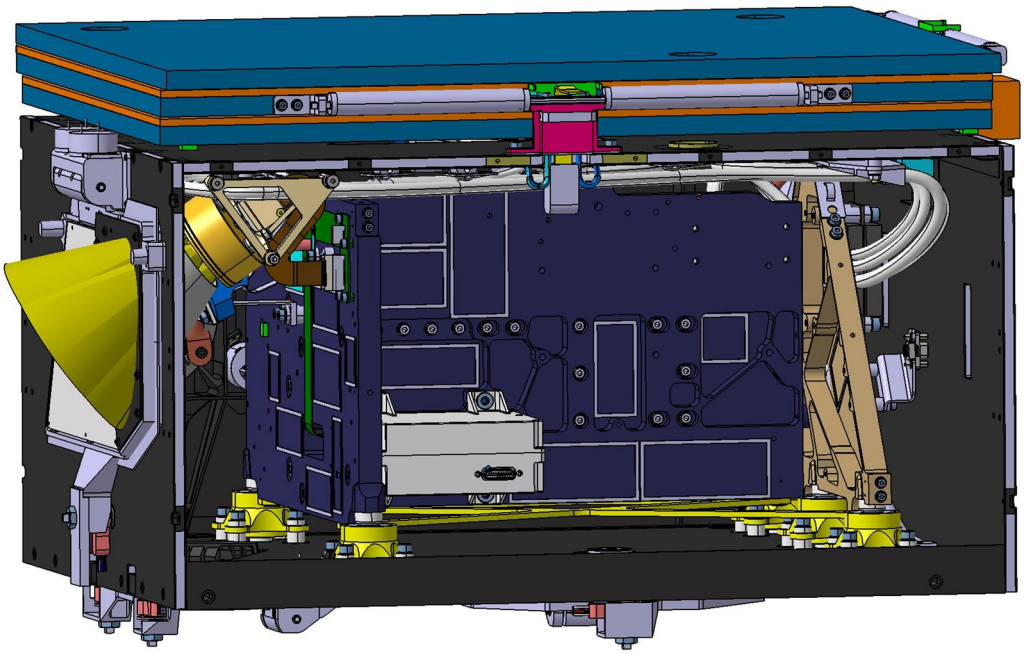

Fig. 1 miniRAD Accommodation: CAD model showing the miniRAD subunits accommodated in the rover structure (wheels and left rover panel removed for view inside). The miniRAD sensor head and mounting bracket are located in the top left corner of the image. The fields of view of the individual sensors are indicated by yellow cones. The instrument is electrically connected to the electronics box via a flexprint cable (brown), which mates with the rigid flex assembly (green) of the electronics subunit. The electronics box (light gray) itself is located inside the rovers's SEM (dark blue). On top (lighter blue) are the solar panels in folded cruise configuration. The miniRAD calibration target (not shown) is mounted on the front shutter (left hand side of the rover) inside the field of view of the sensors

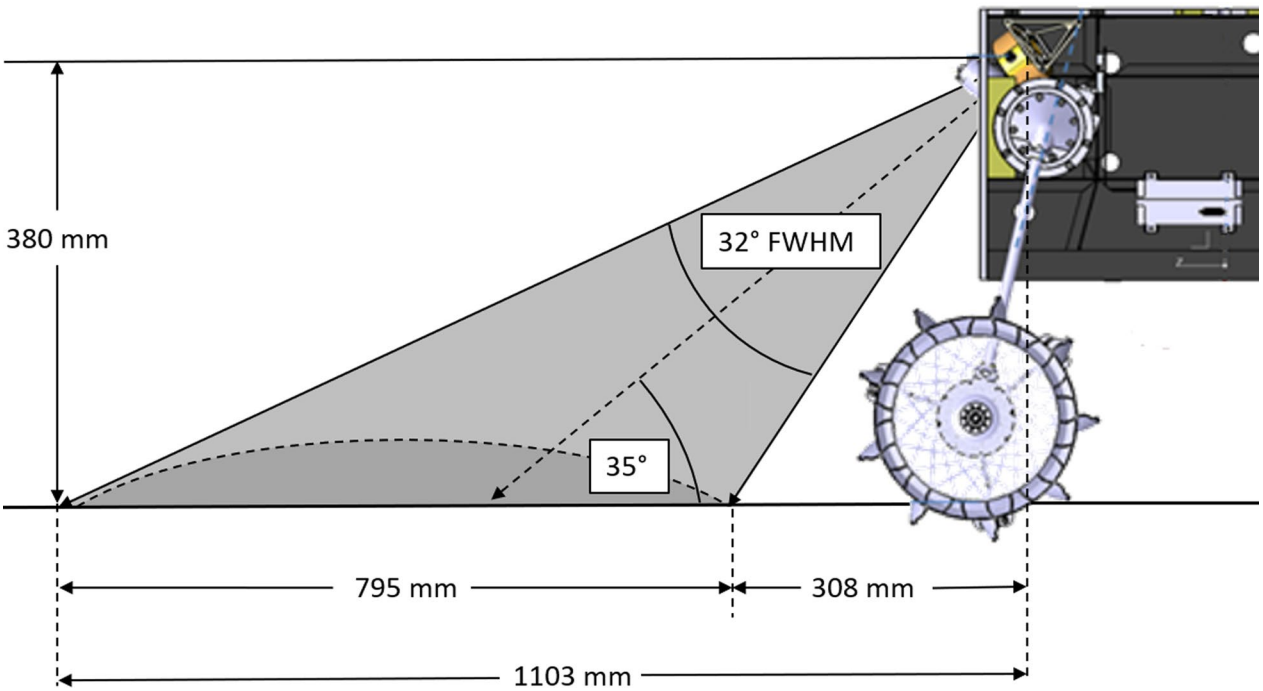

Fig. 2 Sketch of the miniRAD mounting indicating the viewing angles and resulting projected field of view. Given a mounting height of 380 mm, a viewing angle of 35°, and a FWHM field of view of 32°, the skewed elliptical surface footprint has a long axis of 785 mm. At the center, located at a distance of 542 mm, the width of the ellipse is 311 mm. The navigation cameras image the surface from 350 mm to infinity, such that the larger part of the miniRAD field of view is naturally covered by a single exposure of the NavCams without moving the rover (Michel et al. 2022)

Table 2 Instrument Overview: Major engineering budgets as well as the key performance characteristics of the miniRAD instrument

Property		Value	Units
Mass	Sensor head incl. mounting bracket and harness	96	g
	Electronics incl. harness	209	g
	Calibration target incl. harness	27	g
Size	Sensor head incl. mounting bracket	63 × 78 × 83	mm^3
	Electronics	59 × 94 × 90	mm^3
	Calibration target	85 × 95 × 3	mm^3
Ops. temperature range	Sensor head	− 140 to + 50	°C
	Electronics	− 45 to + 60	°C
	Calibration target	− 155 to + 60	°C
Power uptake[a]	Standby mode	0.45	W
	Diagnostic mode	0.55	W
	Science mode	1.0–1.4 W	W
	Calibration mode	4.0	W
Spectral range	Short-wave channels	4.7–6.2	µm
	Narrow bandpass (0.5 µm width)	8.2, 8.9, 9.5	µm
	Long-wave channels	14–25, 15–100	µm
Cal. temperature range	Target temperature	100 to 330	K
Temperature uncertainty[b]	Bandpasses at T > 270 K	1	K
	Long-wave channels at T = 100 K	5	K
NETD[c]	Bandpasses at T = 270 K	6	mK
	Longpasses at T = 100 K	40	mK
Field of view	Full-width half-maximum	32	°
	Total width	45	°
Measurement frequency	Science and calibration mode	0.06	Hz
	Fast science mode	1	Hz
Data rate	Science	72	bit/s
	Housekeeping	45	bit/s

[a] Average power incl. heaters, in sci-mode heater power varies according to the environmental conditions, values for predicted hot/cold environment on Phobos

[b] Temperature uncertainty is a function of the target temperature and spectral channel

[c] *NETD*: Noise equivalent temperature difference

by the rover's common TCS, the external subunits, such as SH and CT, are individually controlled by miniRAD. During operational phases, the SH and CT temperatures are stabilized at their chosen setpoints using a built-in heater and a Pt-100 thermal sensor controlled by the miniRAD electronics, whereas during nonoperational phases, SH and CT passively follow the temperature of the rover environment. Because no active cooling is possible, this approach only works with setpoints above the temperature of the environment. Another objective of the miniRAD TCS is to ensure the required performance (see Table 2) during nominal operational conditions on Phobos and in cruise. The thermal design of the sensor head is driven by the requirement to achieve a high degree of homogeneity and stability in the SH during operational phases, because these parameters have a direct influence on the quality of the elimination of the instrumental background radiation, and, therefore, on the performance of miniRAD. To achieve this goal, and to minimize the heating power required for stabilization, the SH body is thermally decoupled from the rover environment as much as possible. The thermal control concept of the SH employs the following measures:

- Low emissivity coating (gold) of all outer surfaces of the sensor head
- A solid radiation shield also equipped with a low emissivity gold coating
- A low thermal conductivity mounting bracket with low emissivity coating (physical vapor deposited gold)
- Use of a flex harness with thin copper tracks to minimize conductive heat leaks from the SH
- Active heating using a Kapton foil heater glued to the outside of the cylindrical sensor head body.

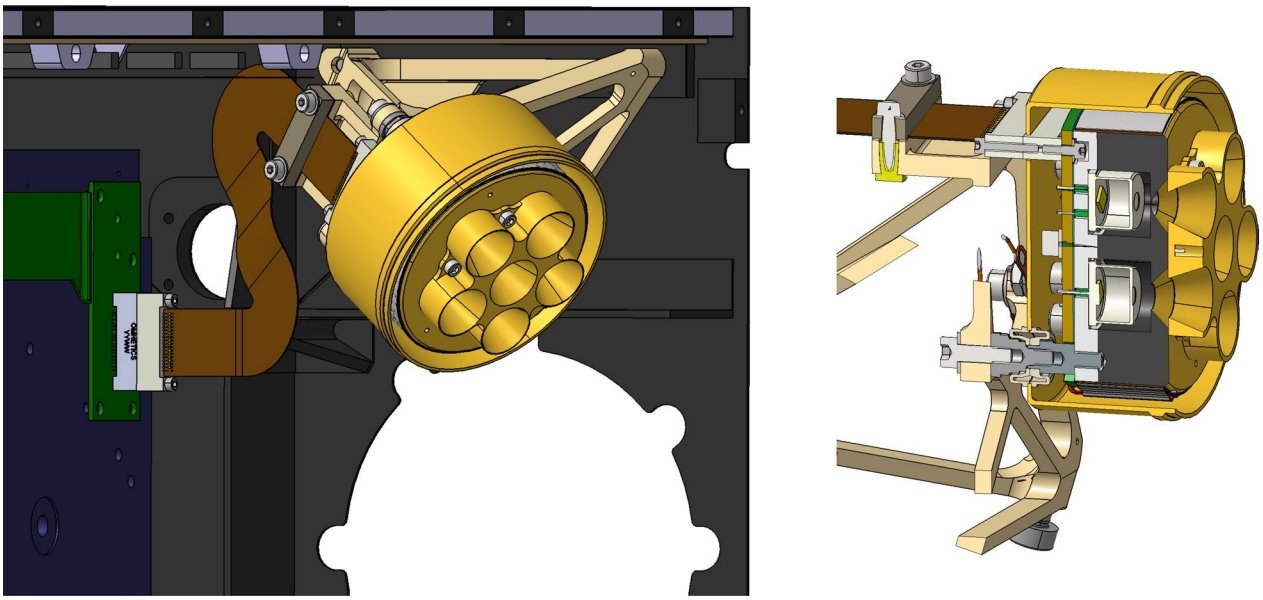

Fig. 3 miniRAD Mounting and Sensor Head (SH): Left: The miniRAD sensor head assembly viewed from the rover front side consisting of sensor head body and radiation cover (gold), a PEEK bracket (beige) mounting the SH to the vertical side panel of the rover (dark gray), and a flexprint (brown) connecting the SH to the electronics unit's rigid flex assembly (green). The white areas arecut-outs in the rover side panel. Right: Cut through the miniRAD sensor head showing the baffle for straylight rejection (right), thermopile detector chips (yellow) mounted on the sockets of TO transistor housings (center), and mounting bracket (left). The sensor head body housing the thermopile detectors is thermally decoupled from its environment by the radiation shield and PEEK bushings, which minimize the conductive path between SH body and radiation shield

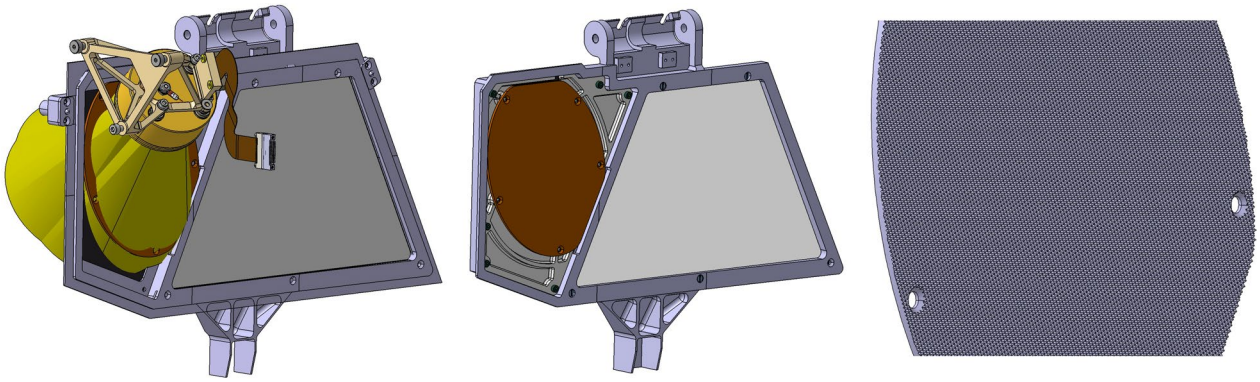

Fig. 4 miniRAD Calibration Target: Left: Backside view of the sensor head and mounting bracket assembly indicating the detector field of view (yellow) and the calibration target (brown) as mounted onto the front shutter (gray). Middle: Calibration target (brown) and insulating PEEK structure (white). Right: Closeup of the calibration target showing the pyramidal microstructures to increase emissivity. Note that the color of the target in the image was chosen for maximum contrast. The flight unit of the target is coated with a high emissivity black coating (see text for details)

- Six thermal sensors of type Pt-100 integrated inside the sensor head body to monitor the thermal state of the SH during operation. One of these sensors can be selected by the miniRAD flight software to serve as control sensor.
- A proportional–integral (PI) controller implemented in the miniRAD electronics controls the necessary heating power to stabilize the SH at the chosen set-point

The main design goal for the calibration target is to serve as a homogenous and high emissivity black-body covering the whole FOV of the miniRAD sensors. To achieve this goal, the CT is coated by Acktar fractal black, a robust and space-proved high emissivity coating.

The already high emissivity is increased further by the pyramidal microstructure of the surface. The Kapton foil heater glued to the backside of the CT provides a maximum power of 2.4 W which is large enough to heat the CT by more than 100 K with respect to the predicted cruise temperature of the rover environment. The temperature of the CT can be controlled by a calibrated Pt-100 glued to the CT backside in a central cut-out of the heater foil. A layer of MLI attached to the backside of the CT minimizes radiation losses to the front shutter. A PEEK support plate provides the mechanical interface to the front shutter while ensuring good thermal isolation from the shutter structure.

3.4 Detectors

The thermopile detectors are modified standard sensors of type TS-72 M from Leibniz-IPHT Jena. The sensor has 72 thermoelement junctions made from the classical thermoelectric material combination $Bi_{0.87}Sb_{0.13}$/Sb connected in series. The sensors use a central terminal, i.e., these sensors are equipped with an additional third electrical terminal for application of a bias voltage which is chosen at the center of the input voltage range of the ADC ($U_{Bias} = 2.5$ V). This design proved its usefulness in sensors used in the MERTIS (Hiesinger et al. 2010) and MARA (Grott et al. 2017) projects, and adapts the sensor circuitry in an optimal way to the differential measurement principle of the miniRAD readout electronics.

The hot junction area of the thermopile sensors can be equipped with different kinds of absorbers. Space flight heritage exists for silver smoke absorbers from MUPUS-TM (Spohn et al. 2007) and MERTIS-RAD (Hiesinger et al. 2010), and also for two variants of interference absorbers used in MARA (Grott et al. 2017) and HP3-RAD (Mueller et al. 2020) which are optimized for one of the two wavelength bands commonly used in thermal imaging, e.g., the short-wave 3–5 µm band, and the long-wave 8–14 µm band. The silver smoke absorbers have a higher absorptance in the long wavelength region beyond 15 µm, but suffer from the drawback that they are rather sensitive to humidity, and, therefore, require either a hermetic package filled with an inert gas (e.g., nitrogen, argon, or xenon) or constant purging during storage on ground. Due to the gas heat conduction, the inert gas filling reduces the sensitivity of the sensor compared to operation in vacuum by a factor of 2–5, dependent on the fill gas. In contrast, the existing interference absorbers have a lower absorptance especially in the long-wave region but are insensitive to atmospheric humidity, which allows the usage in a non-hermetic housing, and the associated sensitivity gain when operated in a vacuum environment. To further increase the performance of the interference absorbers for the measurement of very low target temperatures (Phobos nighttime temperature), a new absorber layer was developed by the detector manufacturer Leibniz-IPHT Jena in close collaboration with DLR for the MMX miniRAD project which extends the high absorptance region to longer wavelengths. The absorptance as a function of wavelength is plotted in Fig. 5. The clear improvement in the wavelength region >20 µm of the newly developed absorber layer (W4) compared to the standard long-wave interference absorber (LW) and also to the silver smoke absorber (Ag) is evident. The new absorber was qualified for flight by an extensive test program consisting of humidity exposure, thermal cycling over the large temperature range required for MMX (100–350 K), and long-term storage in the normal laboratory environment. Repeated measurements of the detector sensitivity during this program did not show any significant changes.

The housing of the sensors is a classical TO-39 transistor housing with a 2.5-mm-diameter aperture hole cut into the top surface of the TO cap, and a 0.2–0.5-mm-diameter venting hole is drilled into the side wall by laser processing, to allow evacuation of the atmosphere when operated under vacuum. The sensor chip is bonded to the TO socket using the space qualified glue Masterbond EP29. The same glue is also used to attach the infrared filters to the inside of the TO caps top surface. The internal electrical connection is made by aluminum wire bonding from bond pads on the chip substrate to the electrical terminals of the TO socket.

3.5 Optical design

The infrared sensors work as a pinhole camera without a dedicated optics, the field-of-view is determined by the aperture holes in the frontplate of the sensor head. An external reflective baffle coated with galvanic hard gold is used to reduce straylight and the exchange of thermal radiation with the environment. The TO-39 housing of each infrared sensor is mounted inside a cylindrical cavity where the walls are coated by a vacuum compatible black paint with high infrared emissivity of 0.97 (Nextel Black Velvet 811-21), another measure to reduce out-of-field straylight.

Six infrared channels with different passbands are realized by optical filters glued to the inside of the TO-39 detector housings. The IR channels of miniRAD are provided in Table 3 and the optical efficiency (the product of blocking window transmittance, filter transmittance, and detector absorptance) is shown in Fig. 6.

Channels TP-2 and TP-4 are dedicated to the measurement of Phobos' surface temperature. The very broadband channel TP-2 is realized with an unusual filter made of pyrolytic boron nitride (BN) (a ceramics instead of the

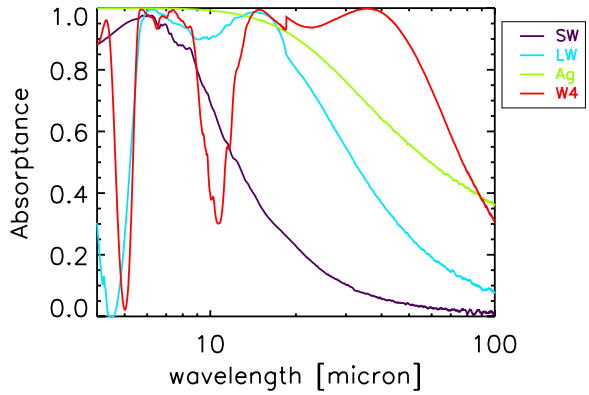

Fig. 5 miniRAD Absorber: Absorptance of different kinds of absorbers as function of wavelength. The miniRAD instrument uses SW, LW, and W4 absorber

usual interference filter) and is optimized for the very low temperatures expected during Phobos' night. It is shown in Fig. 6 that this filter together with the new interference absorbers extends the useful wavelength range of miniRAD to about 100 µm. TP-4 is a Ge LWP filter with a cut-on wavelength of 14 µm which gives larger signal during daytime and less signal during night than the BN filter, thereby mainly improving the miniRAD S/N during daytime. It also adds redundancy for the temperature measurement goal because this channel still gives good signal except for the very low end (100 K) of the expected surface temperature during night. The cut-on wavelength of these filters is selected at a rather long wavelength to minimize the influence of thermal straylight caused by residual thermal gradients inside the detector cavities. Since the SH is operated at temperatures of 273 K or higher, these emissions occur mostly at wavelengths < 14 µm, and, thus, could not reach the detectors.

The three narrowband channels TP-1, TP-3, and TP-6 are standard interference filters on Ge substrate and should be useful for extracting mineralogical information. The wavelength bands around 9 µm were selected to estimate the position of the suspected Christiansen feature using a similar approach as applied by Diviner on NASA's Moon mission LCROSS (Greenhagen et al 2010). To reduce contamination by long-wave out-of-band radiation, these channels are further equipped with additional blocking windows made from CaF_2 which are glued in front of the bandpass filter on a metal ring welded to the front of the TO-39 housings. TP-4 is a long-wave filter on a sapphire substrate where the transmission cutoff of the substrate at about 6.5 µm is effectively providing a broader bandpass at shorter wavelengths which shall be used for the retrieval of information on the small-scale roughness of Phobos' surface.

Table 3 miniRAD Channels: Overview of miniRAD infrared channels giving the channel designation, blocking window material, thermopile absorber, and filter name

Designation	Blocking window	Absorber	Filter
TP-1	CaF2	LW	BP 9480–613 nm
TP-2	–	W4	Ge LWP 14 µm cut-on
TP-3	–	SW	LWP on Sapphire 4.7 µm cut-on
TP-4	CaF2	LW	Ge BP 8248–452 nm
TP-5	CaF2	LW	Ge BP 8900–500 nm
TP-6	–	LW	BN LWP 15 µm cut-on

3.6 Electrical design

The block diagram of the miniRAD electronics is shown in Fig. 7. The digital control of the instrument, heater control, and the analogue data acquisition chain are implemented on a two-PCB Rigid-flex design, an assembly of several PCBs interconnected by flexprint cables. All parts needed for digital control and power conditioning are placed on one PCB, whereas the second PCB accommodates the analogue parts comprising of the analogue signal chains and heater control.

Power supply The necessary power to operate miniRAD is provided by the rover PCDU, two stabilized voltages of 3.3 V and 5 V are used by miniRAD for the digital and analogue parts, respectively. Furthermore, nonregulated bus voltage specified to 11.0–16.8 V is used by miniRAD as supply for the two heaters.

Digital PCB The miniRAD instrument is controlled by a processor implemented in a rad-tolerant flash FPGA of type ProAsic3 from Microsemi. The necessary 1.5 V core voltage is derived from the 3.3 V using a line regulator. The FPGA controls two miniRAD internal heaters (sensor head heater and calibration target heater), the acquisition of samples with three analogue–digital converters (ADCs), and the communication with the

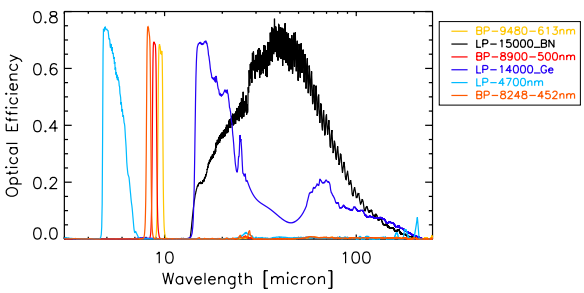

Fig. 6 miniRAD optical efficiency: Optical efficiency as a function of wavelength for the six infrared channels. Details of the employed absorber, filter, and blocking window are summarized in Table 2. Note the excellent rejection of out-of-band radiation for the bandpass filters

Rover on-board computer (OBC) via a RS422 serial link. Default setpoints of both SH and CT are provided by a configuration table, which can be changed by telecommand. No internal mass memory is implemented in the miniRAD design. Therefore, when miniRAD is operating, it needs to be regularly polled by the OBC for the delivery and storage (in the mass memory of the rover) of the acquired data vectors.

Analogue PCB The analogue PCB contains three identical signal processing chains, two for science and one for housekeeping data. Each of these chains consist of eight analogue voltage channels. For redundancy reasons, each scientific ADC acquires signals from three thermopiles and three SH Pt-100 temperature sensors, and additionally from one simulated thermopile and simulated Pt-channel, respectively. In this way, a loss of one ADC would not lead to a total loss of the miniRAD science. The simulator channels are made of precision resistors of 2 × 10 kOhms (for thermopile) and 100 Ohms and are located on the analogue PCB. They provide information on the functionality and stability of the electronics independently from the sensors. Furthermore, the analogue heater control parts, e.g., power FETs, OPAMPs, and passive parts, for control of the SH and CT heaters are located on this PCB.

The small thermopile signal voltages are transferred differentially to the electronics box using the SH flex cable and the flex tail of the electronics and are then converted by a sigma/delta ADC of type ADS1258 with a resolution of 24 Bit. These ADC's incorporate an eight-channel differential multiplexer and have the additional advantage that optimal signal conditioning can be realized using an external user defined circuit. Here, an external differential amplifier is used to provide the necessary high input impedance for the thermopiles with their source resistance of about 20 kOhms and a signal amplification with a gain of G = 11. Due to the placement of the external signal conditioning circuit between MUX output and ADC input, this amplifier can be incorporated into the internal self-calibration feature of the ADS1258, where electrical choppering of the signal is used to reduce offset voltage drifts to a minimum, a feature which is very important

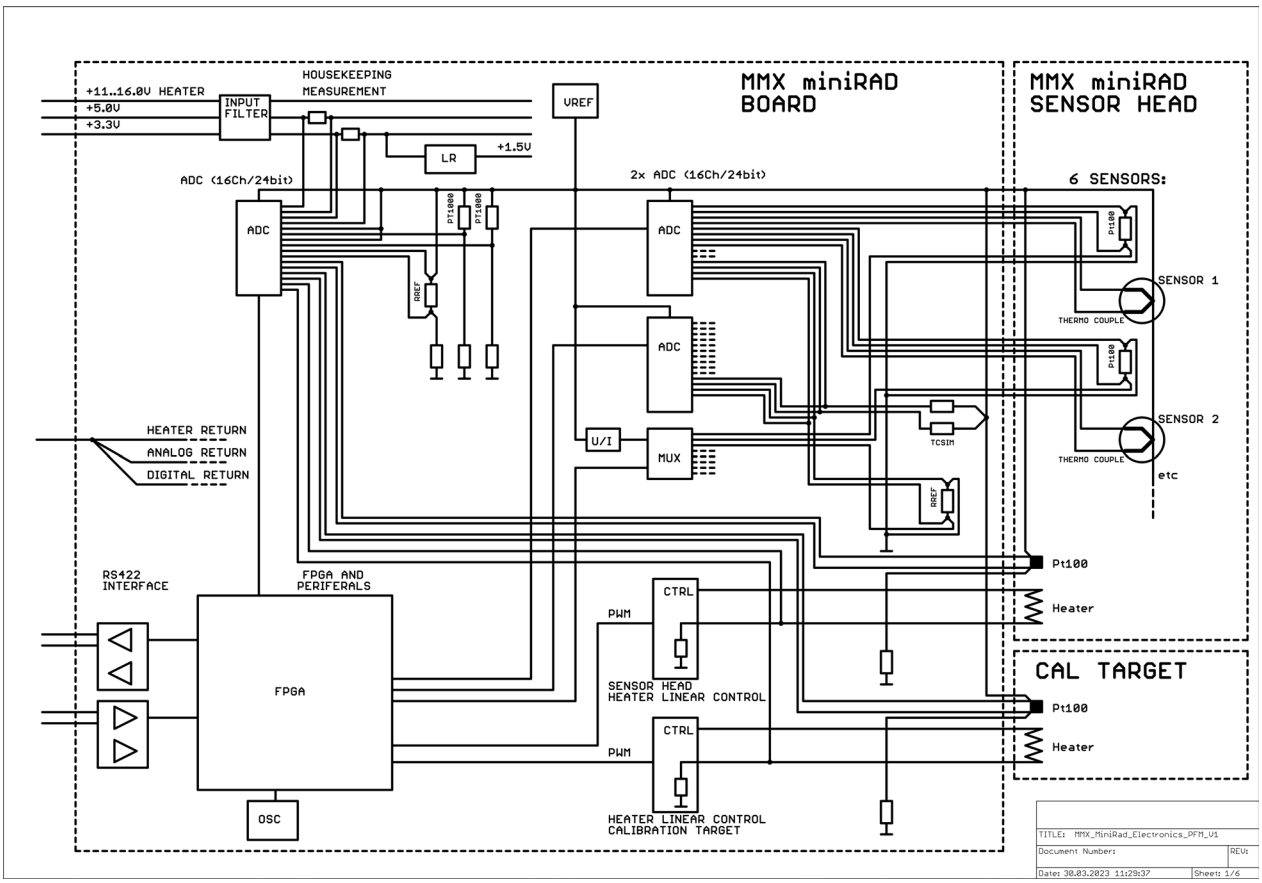

Fig. 7 miniRAD Electronics: Block diagram of miniRAD electronics showing three functional subunits. The main electronics consisting of the digital control unit, temperature control units, housekeeping unit, and analogue chains; the sensor head consisting of thermopile and Pt-100 sensors; and the calibration target consisting of heater and Pt-100 temperature sensor

for the small signal voltages provided by thermopile detectors.

3.7 Operations

During the cruise phase to Phobos, miniRAD will participate in regular Idefix checkouts that shall be performed about every 6 months. In these checkouts, miniRAD inflight calibration mode will be executed where the CT is heated up from the cruise equilibrium temperature, predicted to be about 170 K, in six steps to a maximum temperature of 273 K, thereby covering a large range of the expected surface temperatures on Phobos. Since the CT is mounted in the rover's front shutter that will be opened soon after landing, the last calibration will be performed in orbit around Phobos shortly before rover deployment. The repeated inflight calibrations will allow to detect any possible changes in miniRAD sensitivity or offsets, which might have occurred after the ground calibration, and can be used for corrections, if needed.

Because of thermal reasons Idefix shall land on Phobos' far side. Therefore, no Mars shine needs to be taken into account for the interpretation of miniRAD data. Before a miniRAD operation sequence starts, the rover shall be moved to the foreseen location and attitude. Then, a stereo image shall be acquired by the NAVCAM to verify that the planned target is within the miniRAD field-of-view and to provide context for the measurement. Thereafter, miniRAD science mode shall be executed for a full Phobos rotation of 7:40 h (plus about 30 min in the beginning for SH temperature stabilization at the setpoint) observing the same measurement spot on the Phobos surface while Idefix remains at rest. Operating miniRAD in science mode means that the sensor head works temperature stabilized at one of the calibrated temperature setpoints (0, 25, or 50 °C), and that miniRAD acquires a full science data record comprising six infrared sensor and six sensor head temperature readings every 15 s.

4 Calibration

Calibration of miniRAD comprises three steps starting with calibration of the electronics, followed by the geometrical calibration, and the final radiometric calibration. Each calibration step is described in detail below in the corresponding chapter. Because the miniRAD PFM electronics was required to be delivered early in the project to be compatible with the Idefix rover's integration flow, the PFM electronics was not available any more during the geometric and radiometric calibration of the sensor head. For this reason, the EM-2 (engineering model 2) electronics was calibrated individually in the same way as the PFM and then used for the calibration of the sensor head. The EM-2 has the same design as the PFM, the main differences are the usage of a commercial version of the FPGA and commercial passive components. This approach allows the simple exchange of the electronics boxes by simply replacing the appropriate calibration coefficients in the data reduction.

4.1 Calibration model

The voltage signal U_s of a thermopile detector can be expressed as (Grott et al. 2017):

$$U_s = S(T_{\mathrm{det}})A_d\pi\nu\int_0^\infty H(\lambda)(\varepsilon(\lambda)B(\lambda,T) - B(\lambda,T_{\mathrm{det}}))\mathrm{d}\lambda + U_{\mathrm{OFF,el}} + U_{\mathrm{OFF,th}} \quad (1)$$

with S the sensitivity of the detector in [V/W], A_d the detector area, ν the view factor of the target as seen from the detector, T the target temperature, T_{det} the temperature of the detector, λ the wavelength, H the instrument function (the product of detector absorptance and filter transmittance). $U_{\mathrm{off,el}}$ is an offset voltage generated by the electronics which usually is also dependent on the temperature of the analogue electronics components. $U_{\mathrm{off,th}}$ is a thermal offset coming from residual spatial thermal gradients inside the sensor head that are seen by the detector. Several options exist to approximate Eq. 1 by a function suitable to derive appropriate calibration coefficients. Grott et al. (2017) used a second-order expansion of the sensitivity to deal with the slightly nonlinear behavior of the thermopile signal U_{th} w.r.t net radiative power. Using this method for miniRAD radiometric calibration, data still showed a systematic deviation between fit and data, and generally larger deviations compared to a fit with a modified Sakuma–Hattori equation (Saunders and White 2004), our finally chosen method. After subtraction of the electronics offset (which we remove in a pre-processing step), the equation for the thermovoltage $U_{\mathrm{th}} =$ writes:

$$U_{\mathrm{th}} = R\left[\frac{1}{\exp\left(-\frac{c_2}{AT+B}\right)-1} - \frac{1}{\exp\left(-\frac{c_2}{AT_{\mathrm{det}}+B}\right)-1}\right] + U_0 + c_H P_H \quad (2)$$

where c_2 is the second radiation constant in Planck's law, T a blackbody temperature filling the FOV of the detector, and P_H the sensor head heating power used to stabilize the sensor head at the commanded temperature setpoint. The Sakuma–Hattori fit parameters R, A, and B can be interpreted as responsivity, effective central wavelength, and shift of central wavelength with temperature, respectively. The term $c_H P_H$ is a reasonable first-order approximation for thermally induced signal offsets generated by residual thermal gradients inside the instrument (Grott et al. 2017). It is implicitly assumed that these gradients get stronger when larger heating power is required to stabilize the sensor head. Note that the modified Sakuma–Hattori Eq. (2) representing the miniRAD calibration model relates the measured thermovoltage directly to the blackbody temperature by a Planck-like function with the five fit parameters R, A, and B, U_0, and c_H, thus making the exact knowledge of the instrument function $H(\lambda)$ superfluous for the miniRAD radiometric calibration.

4.2 Electronics calibration

The performance of miniRAD is affected by variations in offset voltage of the different signal channels mainly caused by temperature changes of the analogue chain components. To measure the electronics offset drift as a function of temperature, the integrated miniRAD E-Box was attached via an aluminum adapter plate to a temperature-controlled plate inside a vacuum chamber and connected with flex cable to a sensor head simulator. On top of the assembly, an MLI blanket was placed between the E-Box and the vacuum chamber side walls and top cover. In this way, the thermal environment of the miniRAD E-Box and SH simulator was nearly isothermal during the whole experiment. The SH simulator is made of a PCB mounted on an SH baseplate where the Pt-100 sensors are replaced by fixed 100 Ohms precision resistors and each thermopile is simulated by 2× 10 kOhms precision resistors connected in series and biased in the center by 2.5 V (e.g., the same readout circuit as in the PFM is used). In the ideal case, no current flows through the simulated thermopiles and no voltage is applied; therefore, the voltage signal should be zero for all environmental (and electronics) temperatures.

Seven different cold-plate temperatures between −45 °C and + 50 °C were used for the offset calibration, a temperature range that covers all expected temperatures of the E-Box during miniRAD operations. The resulting offset voltages as function of temperature are plotted in Fig. 8 for the thermopile and the thermopile-simulator channels. In all cases, the offset voltage w.r.t temperature can very well be described by a second-order polynomial with a standard deviation of the fitting residuals of 0.2–0.3 µV.

The same calibration was also performed with the miniRAD EM-2 electronics which was later used for calibration of the sensor head. Qualitatively the results of the EM-2 calibration were similar as for the PFM, although the magnitude of the offset temperature drift was generally lower.

4.3 Geometric calibration

The geometric calibration of a non-imaging radiometer is aimed at determining the total field-of-view (FOV) of a detector and the relative angular sensitivity to incoming radiation. To achieve this purpose, the radiometer was mounted on a precision rotary stage inside a small vacuum chamber such that the absorber of the central miniRAD detector lies on the rotation axis. A sketch of the setup is shown in Fig. 9. The sensor head looks through a 3–12 µm broadband anti-reflection coated ZnSe window which is transparent for infrared radiation on a collimated source of infrared radiation. By rotating the sensor head, the relative sensitivity as function of off-axis angle can then be determined. The source used was a microheater from Axetris of type EMIRS200 AT01 T-BR080, basically a small emitting surface of 2× 2 mm mounted inside a parabolic focusing mirror with an incorporated micro-machined resistive heating element. This type of source has the advantage that it can be electrically modulated by application of a control voltage and has a small thermal time constant of about 15 ms. In our case, the source was driven by a constant voltage which was cycled (switched ON and OFF) N_{cycle} = 10 times at each angular position of the rotary stage. In this way, the varying background contribution to the measured signal

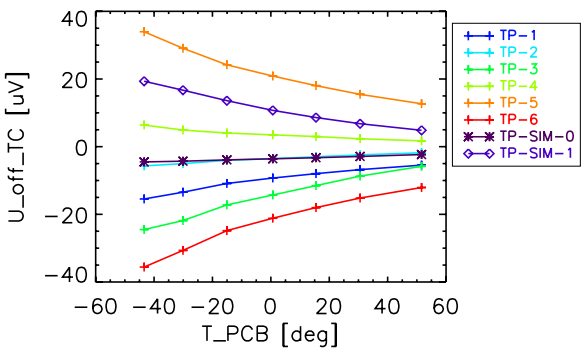

Fig. 8 Thermopile Offset Voltages: Thermopile offset voltages as function of temperature for the individual channels. In the flight unit, channels TP-1 to TP-6 are connected to the sensor head, whereas in this test, they were connected to a sensor head simulator (see Fig. 7). Channels TP-SIM-0 and TP-SIM-1 are reference resistors mounted inside the miniRAD electronics box

(with IR source OFF) could be subtracted from the IR signal and S/N be improved by a factor of $N_{cycle}^{1/2}$. The source is not an ideal collimator but the geometry of the setup with a source aperture of 9 mm and a distance between detector and source of 200 mm gives a maximum divergence of rays falling onto the detector of ± 1.3°, which is deemed acceptable for the present purpose. This assumption has been verified by pretests with the source at larger distances, which showed no significant difference of the results, except for the expected lower S/N.

The results of the geometric calibration are summarized in Fig. 10 which shows the measured relative signal strength for all six infrared channels of miniRAD on the left panel, and the resulting cumulative signal distribution as function of off-axis angle on the right. A closer look at Fig. 10 reveals a somewhat broader angular signal distribution for the BN long-wave pass filters compared to the others. This behavior is probably caused by an increased amount of internal scattering in the ceramics structure of the pyrolytic boron nitride filter, which is absent in the other filters realized as classical interference filters on a Ge substrate. The width of the angular sensitivity distribution can be characterized by the full-width half-maximum (FWHM) which lies between 30° and 34° for the different filters and the contribution of the nominal FOV of 45° to the total signal is about 97–98%.

4.4 Radiometric calibration

Radiometric calibration of infrared radiometers based on thermopile detectors can be performed in different ways. Sebastián et al. (2020) used a combination of a relative calibration of the detector sensitivity as function of sensor temperature and a single absolute calibration run performed at a sensor temperature of 313 K for the MEDA-TIRS radiometer on the perseverance rover of NASA. This method assumes that any nonlinearity of the infrared sensor can be neglected. Note here that even for the case of a perfectly linear thermopile detector, an apparent nonlinearity could still result from uncertainties in the measurements of the instrument function or from non-negligible absorption and re-emission from the infrared filters (Christensen et al. 2024). Because our experience with previous projects showed that slight nonlinearities of the sensors cannot be excluded, we choose the approach already used by Grott et al. (2017) for the calibration of MARA which also follows as closely as possible the widely accepted general rule "calibrate as you measure" (Wolfe 1998). The calibration was carried out in high vacuum, with relevant thermal boundary conditions based on predictions of the thermal environment for miniRAD operations on Phobos, and blackbody temperatures covering the full expected object temperature range.

The radiometric calibration of miniRAD was performed in the space simulation facility (a thermal vacuum chamber) at DLR, Berlin, using a low temperature cavity blackbody of type BB-100 (Sapritsky et al 2003) which can be attached to a flange in the front door of the TV chamber. This blackbody can be cooled by LN_2 and has an operational temperature range of 100–400 K, and

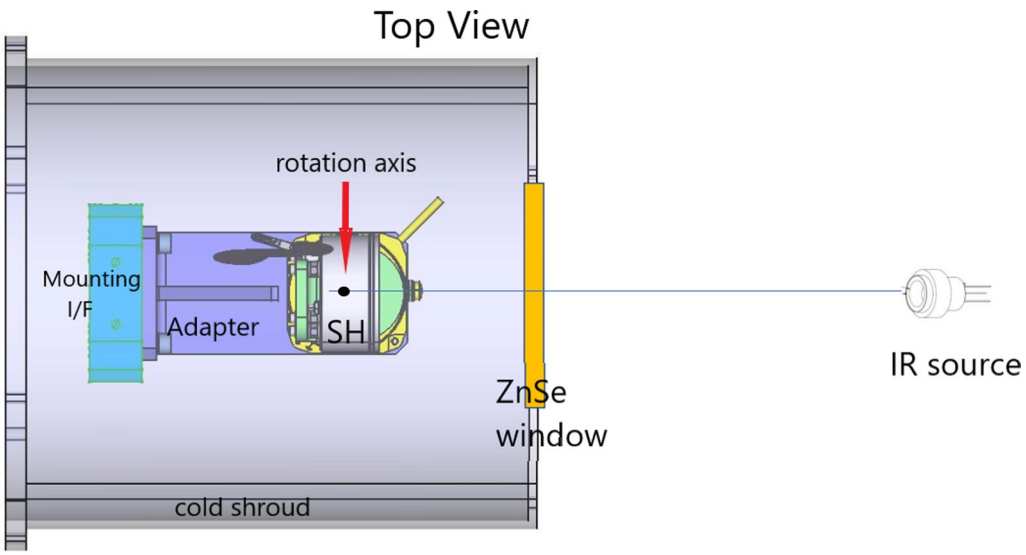

Fig. 9 Geometrical Calibration Setup: Sketch of the experimental setup for geometrical calibration with the sensor head in the 0° position, directly facing the source (viewed from top). In the figure, the rotation axis is out of plane and its location is indicated. While the rotary stage and sensor head are mounted inside a thermal vacuum chamber, they view the infrared source located outside the chamber through an IR transparent ZnSe window

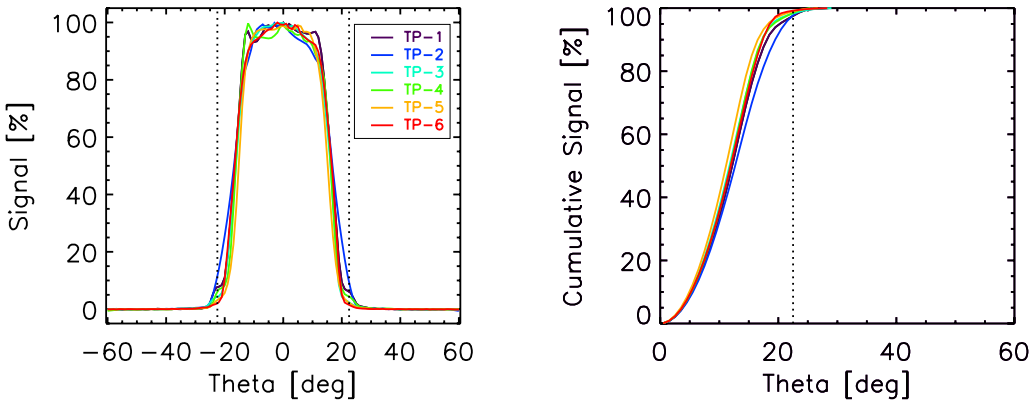

Fig. 10 Geometrical Calibration Results: Left: Normalized signal as a function of off-axis angle Theta for the individual miniRAD channels. Right: Cumulative signal as a function of off-axis angle Theta for the individual miniRAD channels. The nominal field of view of 22.5° is indicated by dotted lines. Overall, about 98% of the total signal is originating from within ± 22.5°

an emissivity of 0.999. The high emissivity is achieved by a combination of the blackbody's V-grooved backplate (Prokhorov et al. 2003) and a specially designed reflective baffle. An overview of the radiometric calibration setup is given in Fig. 11. Because of the large FOV of miniRAD, the sensor head had to be placed directly in front of the blackbody aperture with a diameter of 100 mm. The sensor head is mounted inside a thermally controlled aluminum enclosure aimed at simulating the real thermal environment for the operational conditions of the sensor head. To achieve the relevant environment temperatures of the SH predicted for the mission in the range between − 120 and 50 °C, the backplate of the enclosure is connected by an aluminum strut to a cold-plate cooled by LN_2. Temperature sensors and Kapton foil heaters placed on the support strut are then used to deliver the required temperature to the SH enclosure. The enclosure itself is further equipped with several temperature sensors and smaller heaters which can be used additionally to modify the spatial temperature distribution of the enclosure, thereby modifying the radiative environment of the sensor head. The electronics is also mounted by a support structure to a position roughly in the center of the strut. The E-Box support is also temperature-controlled by an incorporated fluid reservoir which is connected to a Huber bath thermostat. The electrical connection between the SH and the E-Box is made by the flight-model flexprint of the SH which is directly plugged into the nano-D receptacle of the interface PCB of the electronics Rigid-flex tail. This interface PCB is fixed with stainless steel standoffs to a small aluminum plate which represents the front panel of the SEM. This interface plate is also equipped with a temperature sensor and a small heater in TO-220 case in order to provide a realistic operational temperature on this thermal interface of the sensor head.

The miniRAD SH was calibrated at three operational setpoints of 0 °C, 25 °C, and 50 °C which are compatible with the thermal predictions for operations on Phobos and during cruise. On each SH setpoint, at least one sensitivity and an offset calibration run were performed. A sensitivity calibration run is performed in the following way. First, the blackbody is cooled down to a minimum temperature below 100 K. In parallel, the temperature of the thermal enclosure is selected and stabilized at the chosen "environment" setpoint. Then, the selected miniRAD SH setpoint is commanded and, depending on the initial temperature, the sensor head is heated up and then stabilizing at its operational temperature setpoint. Once miniRAD and thermal enclosure are both in stabilized conditions, a table of blackbody setpoints is loaded by the blackbody control software, and the calibration run starts. In total, 10 BB setpoints were used to cover the range from 100 to 330 K.

Another type of calibration run is the offset calibration which shall take into account the different environmental conditions the radiometer may encounter during the operations on Phobos. Here, the blackbody is held stable at a temperature as close as possible to the SH operational temperature (ideally resulting in a zero signal) while the temperature of the environmental box is varied, typically in five steps over the relevant temperature range of about several 10 K. As a consequence of the changing thermal environment, the SH heater power required to maintain the setpoint temperature varies accordingly. The main purpose of the offset calibration runs is to provide good constraints on the heater power coefficient c_H in Eq. 2. Using all acquired calibration points, a

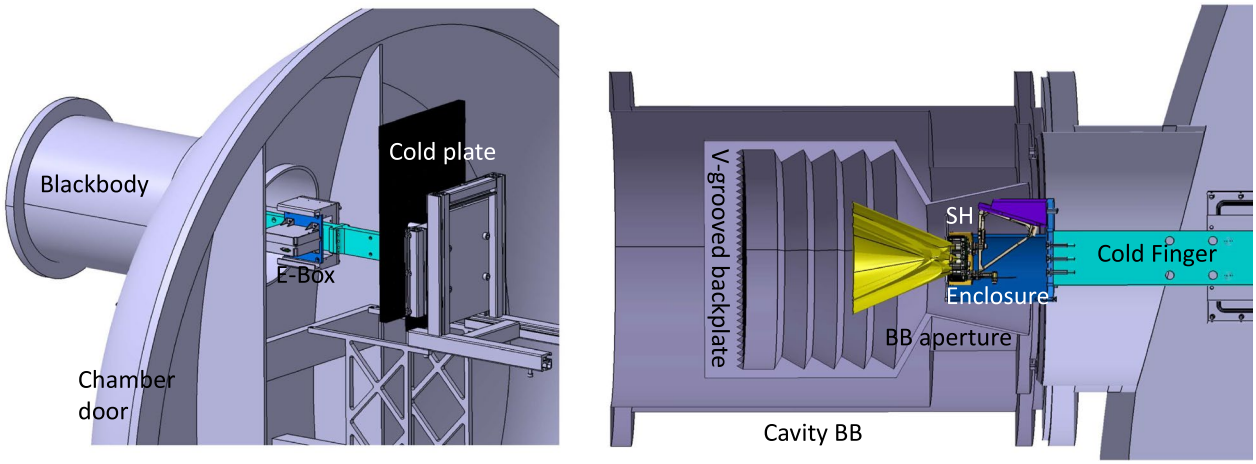

Fig. 11 Radiometric Calibration Setup: Left: CAD model of the calibration setup inside the thermal vacuum chamber. The cavity blackbody is located to the left and the miniRAD instrument is mounted close to the blackbody aperture. It is connected to a temperature-controlled plate (black) via aluminum struts acting as cold finger (light blue). The miniRAD electronics box (gray box on dark blue mounting plate) is mounted close to the sensor head on the struts. Right: Cut view of the assembly showing the cavity blackbody with its V-grooved backplate on the left, the miniRAD sensor head (gold) and sensor field of view (yellow), the thermal enclosure (blue) as well as the cold finger (light blue)

least-squares fitting routine is applied to find the best fitting five parameters in the governing Eq. (2).

An example of the acquired data during a blackbody calibration run is provided in Fig. 12, where the right panel shows the blackbody temperature varying from 85 to 330 K in 10 steps (85, 100, 120, 150, 180, 210, 240, 273, 300, 330 K) and the left panel shows the resulting thermopile voltage of the six infrared miniRAD channels. Each blackbody setpoint has a duration of 1 h, enough time for blackbody and sensor head to reach a sufficient thermal equilibrium. The data acquired during the last 10 min at each BB setpoint is then averaged and used as a calibration point in the fitting model according to Eq. (2).

The result of the radiometric calibration at the SH temperature setpoint of 0 °C is plotted in Fig. 13, showing the thermopile voltage data points (symbols) and the corresponding fit results (solid lines) on the top panel, the deviation of fit from data in [μV] in the central panel, and the corresponding deviation of brightness temperature from blackbody temperature on the bottom panel. At this SH setpoint, two sensitivity calibration runs were performed with different settings for the enclosure temperature of − 50 °C and − 100 °C, respectively. All calibration points of two sensitivity and one offset calibration run are plotted in Fig. 13.

As expected, the largest signals are generated by the two broad LWP filters (light and dark blue curve in left panel). The deviation of fit from data is of the order of 1–2 μV, with the exception of the short-wave LP-4700 which shows somewhat larger fitting residuals. The resulting deviations between inverted brightness and blackbody temperatures are low (below 0.5 K) and nearly random above a certain lower limit temperature which is different for each infrared channel, as can be expected from the different passband width and upper wavelength cutoff of the different filter functions. This lower limit temperature is about 85 K for the BN and LP-14 filters, 180–210 K for the three bandpass filters and about 240 K for the short-wave filter (LP-4700, 4.7–6.2 μm). It is worth noting that the calibration points from the two sensitivity runs plot well on top of each other, so good that the subtle differences can only be seen in the residual plots in the center and lower panel of Fig. 13. The result shown in Fig. 13 is typical for the radiometric calibration, the fitting residuals for the other two sensor head setpoints at 25 °C and 50 °C are similar.

4.5 Verification of calibration

The fitting residuals of the radiometric calibration discussed above suggest that the uncertainty of the miniRAD brightness temperature measurements are below 1 K even at the low end (< 100 K) of the target temperature range, but this is probably over-optimistic. There are several reasons why the situation could be worse during real operations on Phobos' surface. The first point is that the calibration points were taken in a steady state, while during real operations, the thermal environment is permanently changing giving rise to changing heating power needed to maintain the setpoint, with the consequence of residual thermal gradients developing in the sensor head. Furthermore, the enclosure was quite homogeneous (within 15 K) in temperature during calibration, whereas the real thermal environment might have a considerably larger inhomogeneity, which also

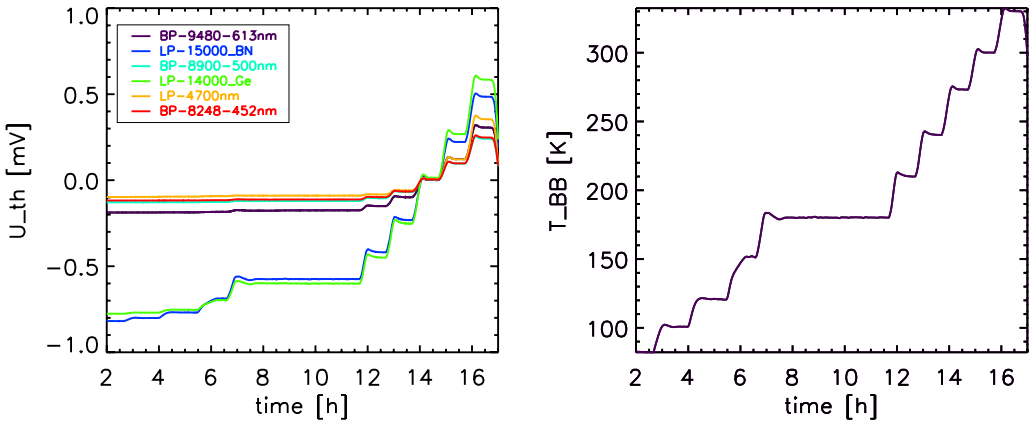

Fig. 12 Radiometric Calibration Data: Data obtained during radiometric calibration showing (left) recorded thermopile voltages as a function as well as (right) the corresponding blackbody temperature as a function of time. The data shown was acquired during one blackbody calibration run using a sensor head setpoint of 0 °C and an environmental temperature of $T_{env} = -50$ °C

might cause slightly different temperature gradients in the sensor head during calibration and operation.

In order to get a better estimate of the real performance, we conducted several verification runs with different experimental setups. First, we checked the repeatability of the radiometric calibration setup by applying the calibration coefficients determined with the final setup to a sensitivity calibration run performed with a similar preliminary setup. During the preliminary sensitivity run with this setup, we observed temporarily increased noise on the thermopile signals (caused by a small contact between SH flex and enclosure as inspection later showed) and we decided to completely rework the setup. Although the sensor head temperature control was not optimal in the first setup, the added noise was low enough that the measurements are still useful. The result of the brightness temperature inversion for the preliminary setup is shown in Fig. 14. The very broadband LP-15000_BN filter gives very good agreement over the whole temperature range, whereas the LP-14000_Ge is not usable below 100 K, but performs well above 120 K. The three narrow bandpass filters with central wavelengths around 9 µm show good agreement for temperatures above 200 K, whereas the short-wave LP-4700 filter is good above 230 K.

Then, we simulated transient and nonhomogenous thermal environmental conditions by varying the enclosure temperature and homogeneity by using the auxiliary heaters on the thermal enclosure for that purpose. The main result from this test was that the brightness temperature inversion was robust against the environment changes, overall the deviations from the blackbody temperature were even smaller than for the repeatability test described before. In a further test, we varied the temperature of the SH flexprint at the interface PCB of the electronics between − 25 and 50 °C while keeping the blackbody temperature constant at 273 K. Here, we found only small changes of signal voltages less than ± 0.5 µV for all signal channels, again smaller than the repeatability uncertainty.

The final check of radiometric calibration was performed with a completely different setup in a cryostate (a small vacuum chamber equipped with a two stage Gifford–McMahon He cooler) of the thermal laboratory of DLR, Berlin. This setup is shown in Fig. 15. The cold finger interface (red) of the second stage of the cryocooler provides the temperature (down to 50 K possible) which is transferred to a custom blackbody (black) via an aluminum adapter plate (blue). The first stage of the cryocooler is thermally well coupled to the chamber's cylindrical cold shield (light brown), meaning that very low temperatures can be reached inside the whole chamber. The cryostate is also equipped with two internal cartridge heaters (one for each stage), but these are not strong enough to provide the highest blackbody temperatures required for calibration. Therefore, an additional aerial Kapton foil heater is mounted between adapter plate (blue) and the backside of the blackbody for this purpose. To provide a high effective emissivity of the blackbody, the radiation surface is coated with 3 M Nextel black velvet 811–21 paint, a well-characterized coating for vacuum blackbodies with a normal emissivity of about 0.97 (Lohrengel and Todtenhaupt 1996; Adibekyan et al. 2017), and also structured with V-shaped grooves to further increase the effective emissivity to values in the range 0.99–0.995 (according to Prokhorov et al. 2003 for the blackbodies groove vertex angle of 30°).

The miniRAD SH is mounted inside a temperature-controlled aluminum box and observes the blackbody from a short distance, such that the large FOV is fully

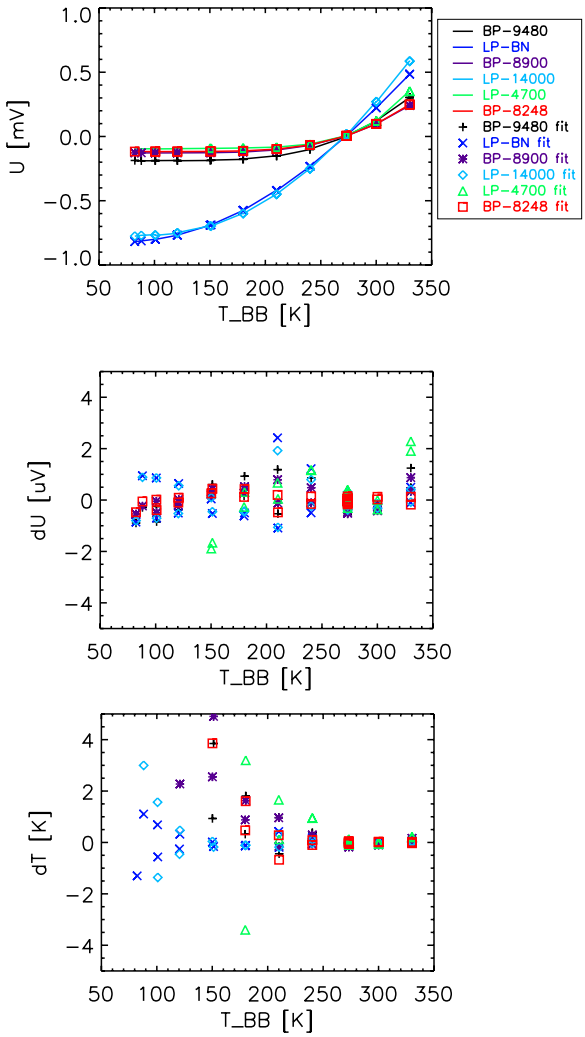

Fig. 13 Radiometric Calibration Results: miniRAD calibration results for a sensor head setpoint of 0 °C. Top: Thermopile voltages (solid lines) recorded during the equilibrated blackbody temperature plateaus as a function of blackbody temperature for the six miniRAD infrared channels. The best fitting curves using the Sakuma–Hattori equation (Eq. 2) are shown as symbols. The plot contains all points from two sensitivity and one offset calibration runs. Middle: Fitting residuals between recorded data and best fitting Sakuma–Hattori model as a function of blackbody temperature. Bottom: The deviation of inverted brightness temperature from blackbody temperature corresponding to the misfit shown in the middle panel as a function of blackbody temperature

covered by the blackbody. This box is aimed at representing the different operational thermal environments of the SH on Phobos and during cruise. The box is at its rear face thermally weakly coupled to the cold shroud by a flat PEEK ring, and is equipped with heaters on several sides of the box. This setup allows to reach all relevant environmental temperatures from 170 to 300 K.

Because of space constraints inside the chamber, the miniRAD electronics was placed outside of the chamber close to the feedthrough in the front flange. The miniRAD flex cable needed an extension cable (shielded round wire cable) inside the chamber to reach the chamber feedthrough and another short cable of the same type was also needed outside to feed the signals into the E-Box.

Two sensitivity runs at the most relevant sensor head temperatures of 0 °C and 25 °C were conducted to check the radiometric calibration of miniRAD. The results are plotted in Figs. 16 and 17 where a constant blackbody emissivity of 0.99 was assumed. The thermal boundary conditions (enclosure temperature, flex interface temperature) for the T_{SH} = 0 °C run were bracketed by the boundary conditions employed during radiometric calibration, while for the T_{SH} = 25 °C run, the thermal boundary conditions were intentionally chosen to be outside of the calibrated range to simulate a worst case. In this case, both, the enclosure temperature (190 K vs. 240 K) and the flex interface temperature (210 K vs. 280 K) were significantly lower than during the calibration run which resulted in higher SH heating power required to maintain the setpoint and the associated increase of thermal gradients inside the sensor head.

The test at T_{SH} = 0 °C shows good agreement between inverted brightness and blackbody temperature for the two broadband channels over the full target temperature range of 100–330 K. Even at the lowest temperature of 100 K, the deviations were less than 3 K. All channels give good results within 1 K deviation from the blackbody for temperatures >270 K, the expected dayside temperatures on Phobos. For the 25 °C setpoint, the results are less good, but still acceptable, especially if one takes into account that this test could be considered as (a probably unrealistic) worst case. The deviation at a blackbody temperature of 100 K increases to 6 K for the boron nitride longpass filter (LP-15000_BN) and is twice as large for the Ge 14 µm cut-on filter (LP-14000_Ge), but this filter also gives useful results with deviations < 5 K for T > 120 K. Generally, all channels show a trend of negative deviations increasing in magnitude with decreasing temperature. This behavior is qualitatively consistent with a shift in offset voltage between the calibration check setup and the radiometric calibration.

Such offset shifts may also occur under real operational conditions on a space vehicle for several reasons. One reason could be that the thermal simulation of the operational environment during calibration may not be fully representative, despite our efforts to simulate them as good as possible in the laboratory, or long-term drift of the electronics may shift the offset voltages by some µV.

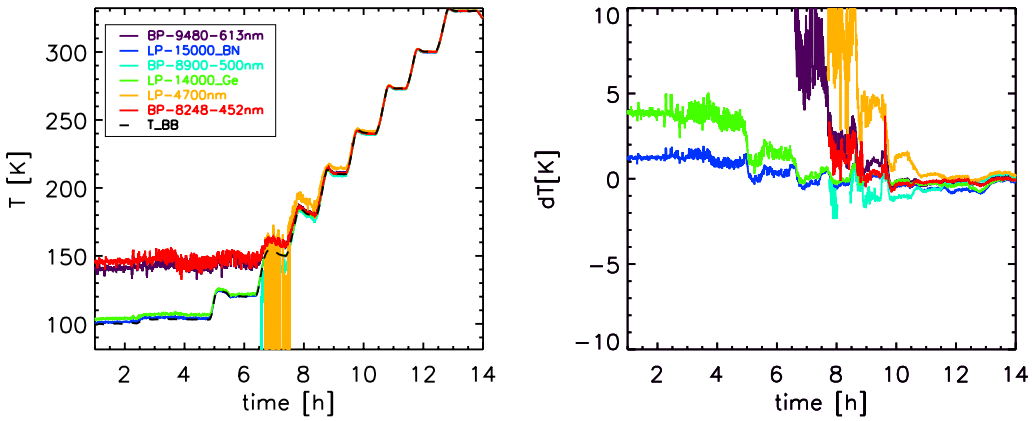

Fig. 14 Verification Measurements: Left: Inverted brightness temperature as a function of time during the verification measurement using the preliminary setup. Right: The deviation of inverted brightness temperature from blackbody temperature as a function of time during the same test

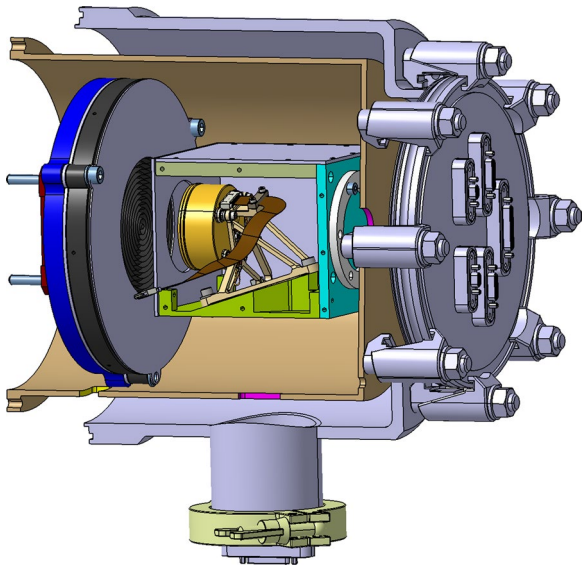

Fig. 15 Radiometric Calibration Verification Setup: CAD model of the radiometric calibration verification setup. The coldfinger (red) controlling the blackbody (gray) temperature is located to the left, the miniRAD sensor head (gold) is mounted inside the thermally controlled enclosure viewing the blackbody. The entire setup is housed in a vacuum chamber and radially decoupled from the environment by the chamber's cold shield (brown)

5 Summary and conclusion

The DLR/CNES rover Idefix, on-board JAXA's MMX mission to Phobos, carries as payload the radiometer miniRAD. MiniRAD was designed, built, and calibrated at the DLR Institute for Planetary Research from 2019 to 2022 and delivered to the Idefix project in 2022, first the electronics box in May 2022, and then the sensor head in Dec 2022. The six-channel radiometer miniRAD is equipped with two broadband filters for measurement of the diurnal temperature curve, three narrow bandpass filters centered around 9 µm for mineralogical characterization based on the Christiansen feature detection, and a short-wave bandpass for constraining the surface roughness of Phobos.

The instrument was calibrated over the full relevant target temperature range from 100 to 330 K at three different sensor head temperature setpoints of 0, 25, and 50 °C. Because of the early delivery of the E-box to the project, the sensor head calibration had to be carried out with a functionally equivalent E-box engineering model. Slightly different electrical properties of the electronics models which may influence the miniRAD performance, especially the offset voltage drift w.r.t. temperature, were accounted for by individually calibrating both electronics over the full operational temperature range in a vacuum chamber. Uncertainty of this calibration, or thermal differences of the real operational environment w.r.t calibration environment may lead to shifts in offset voltages, but these will be detected during the planned inflight calibration runs in cruise, and could then be corrected. In addition to the calibration, extensive verification of the radiometric calibration has been performed with good results. Therefore, we predict a brightness temperature uncertainty at the 2-sigma level of < 1 K for all channels at typical dayside temperatures > 270 K, and an uncertainty of < 5 K at 100 K for the broadband LP-15000_BN filter. This gives confidence that the miniRAD performance is sufficient to reach all scientific goals detailed in the science traceability matrix (Table 1).

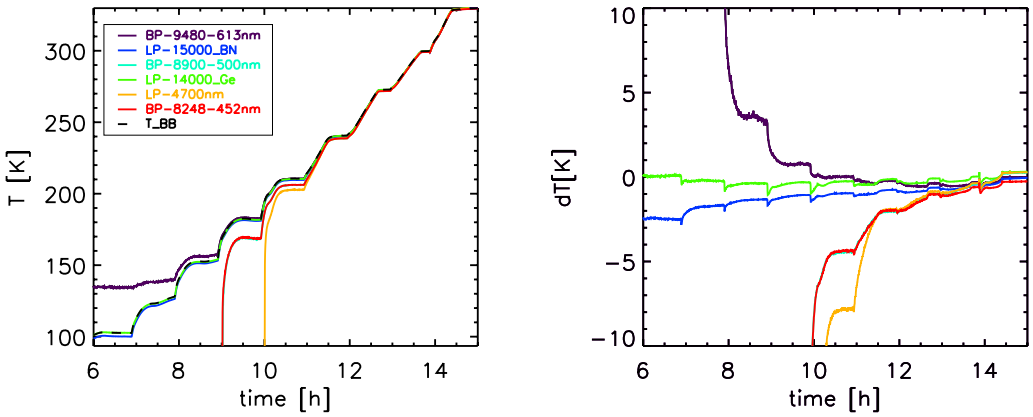

Fig. 16 Radiometric Calibration Verification Results at 0 °C: Left: Inverted brightness temperature for the six miniRAD channels as well as commanded blackbody temperature as a function of time during the verification experiment. Right: Deviation of inverted brightness temperature from blackbody temperature as a function of time. The sensor head setpoint was commanded to T_{SH} = 0 °C

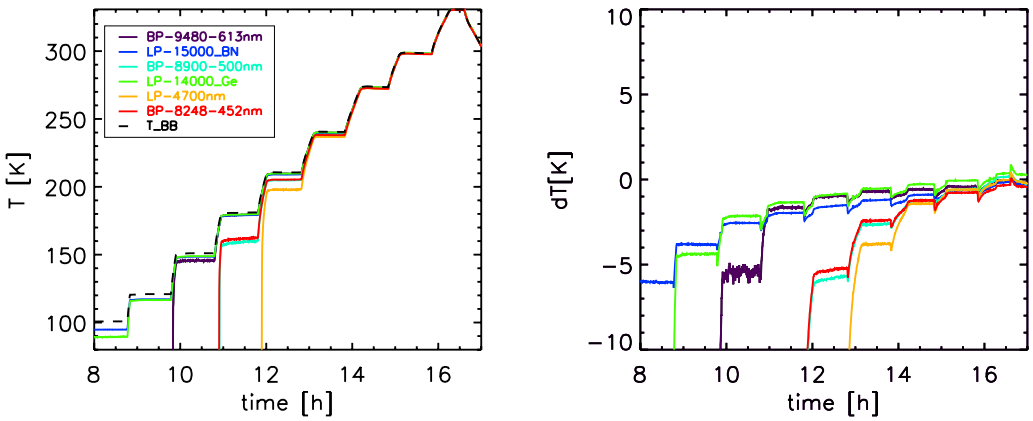

Fig. 17 Radiometric Calibration Verification Results at 25 °C: Same as in Fig. 16, but for a sensor head setpoint of T_{SH} = 25 °C

Abbreviations

BB	Blackbody
BN	Boron nitride
CNES	Centre National d'Etude Spatial (French space agency)
CT	Calibration target of miniRAD
DLR	Deutsches Zentrum für Luft- und Raumfahrt (German space agency)
EM	Engineering model
FOV	Field-of-view
Idefix	DLR/CNES rover, payload on MMX mission
JAXA	Japan Aerospace Exploration AgencyAerospace eXploration Agency
MMX	Martian Moons eXploration
MiniRAD	Radiometer payload on IDEFIX
MLI	Multi layer insulation
NAVCAM	Navigation camera payload on IDEFIX
PEEK	Poly-ether-ether-ketone (space-proved polymer)
PFM	Proto flight model
SEM	Structural and electrical module (inner compartment of Idefix)
SH	Sensor head of miniRAD

Acknowledgements
The rover on the MMX mission of JAXA is a CNES-DLR cooperation. The authors would like to thank the whole MMX team at JAXA/ISAS for the unique opportunity to participate to this exciting mission. The authors would like to thank the two reviewers for their efforts which improved the quality of the manuscript.

Author contributions
J. Knollenberg and M. Grott conceived and designed the miniRAD instrument. J. Knollenberg and M. Grott prepared the first draft of the paper. M. Hamm, A. Ihring, R. Ziese, and J. Biele provided comments on the manuscript draft and participated in discussions. All authors read and approved the final manuscript.

Funding
Open Access funding enabled and organized by Projekt DEAL. This research has been funded by DLR.

Availability of data and materials
All data used in this publication will be made available upon reasonable request to the corresponding author.

Declarations

Competing interests

The authors declare that they have no competing interest.

Received: 16 November 2024 Accepted: 22 May 2025
Published online: 14 July 2025

References

Adibekyan A, Kononogova E, Monte C, Hollandt J (2017) High-accuracy emissivity data on the coatings: Nextel 811–21, Herberts 1534, Aeroglaze Z-306, Acktar Fractal Black. Int J Thermophys 38:89. https://doi.org/10.1007/s10765-017-2212-z

Bandfield JL, Piqueux S, Glotch TD, Shirley KA, Duxbury TC, Hill JR, Edwards CS, Plaut JJ, Hamilton VE, Christensen PR (2018) Mars Odyssey THEMIS observations of phobos: new spectral and thermophysical measurements. Paper presented at the 49th lunar and planetary science conference 2018, (LPI Contrib. No. 2083)

Biele J, Kührt E, Senshu H, Sakatani N, Ogawa K, Hamm M, Grott M, Okada T, Arai T (2019) Effects of dust layers on thermal emission from airless bodies. Prog Earth Planet Sci. https://doi.org/10.1186/s40645-019-0291-0

Biele J, Grott M, Zolensky ME, Benisek A, Dachs E (2022) The specific heat of astro-materials: review of theoretical concepts, materials, and techniques. Int J Thermophys. https://doi.org/10.1007/s10765-022-03046-5

Christensen PR, Spencer JR, Mehall GL, Patel M, Saadat A, Brick M, Bowles H, Farkas Z, Fisher T, Gjellum D, Holmes A, Kubik I, Larson M, Levy M, Madril E, Masini P, McEwen T, Miner M, Nickles N, O'Donnell W, Ortiz C, Osterman D, Pelham D, Rudeen A, Saunders T, Woodward R, Abramov O, Hayne PO, Howett CJ, Mellon MT, Nimmo F, Piqueux S, Rathbun JA (2024) The EUROPA mission Thermal Imaging System (E-THEMIS) Investigation for the Europa Clipper mission. Spac Sci Rev 220:38. https://doi.org/10.1007/s11214-024-01074-1

Cooper BL, Salisbury JW, Killen RM, Potter AE (2002) Midinfrared spectral features of rocks and their powders. J Geophys Res Planets 107(E4):5017. https://doi.org/10.1029/2000JE001462

Davidsson BJR, Rickman H (2014) Surface roughness and three-dimensional heat conduction in thermophysical models. Icarus 243:58–77

Delbo M, Libourel G, Wilkerson J, Murdoch N, Michel P, Ramesh KT, Ganino C, Verati C, Marchi S (2014) Thermal fatigue as the origin of regolith on small asteroids. Nature 508(7495):233–236. https://doi.org/10.1038/nature13153

Giese B, Kuehrt E (1990) Theoretical interpretation of infrared measurements at Deimos in the framework of crater radiation. Icarus 88:372–379. https://doi.org/10.1016/0019-1035(90)90088-Q

Greenhagen BT, Lucey PG, Wyatt MB, Glotch TD, Allen CC, Arnold JA, Bandfield JL, Bowles NE, Hanna KL, Donaldson HPO, Song E, Thomas IR, Paige DA (2010) Global silicate mineralogy of the moon from the diviner lunar radiometer. Science 329:1507. https://doi.org/10.1126/science.1192196

Glotch TD, Edwards CS, Yesiltas M, Shirley KA, McDougall DS, Kling AM, Bandfield JL, Herd CDK (2018) MGS-TES spectra suggest a basaltic component in the Regolith of Phobos. J Geophys Res Planets 123(10):2467–2484. https://doi.org/10.1029/2018JE005647

Grott M, Knollenberg J, Hamm M, Ogawa K, Jaumann R, Otto KA, Delbo M, Michel P, Biele J, Neumann W, Knapmeyer M, Kührt E, Senshu H, Okada T, Helbert J, Maturilli A, Müller N, Hagermann A, Sakatani N, Tanaka S (2019a) Low thermal conductivity boulder with high porosity identified on C-type asteroid (162173) Ryugu. Nat Astron 3:971–976. https://doi.org/10.1038/s41550-019-0832-x

Grott M, Knollenberg J, Borgs B, Hänschke F, Kessler E, Helbert J, Maturilli A, Müller N (2017) The MASCOT radiometer MARA for the Hayabusa2 mission. Space Sci Rev 208:413–431. https://doi.org/10.1007/s11214-016-0272-1

Grott M, Knollenberg J et al (2019b) Low thermal conductivity boulder with high porosity identified on C-type asteroid (162173) Ryugu. Nat Astron 3:971. https://doi.org/10.1038/s41550-019-0832-x

Grott M, Biele J, Michel P, Sugita S, Schröder S, Sakatani N, Neumann W, Kameda S, Michikami T, Honda C (2020) Macroporosity and grain density of rubble pile asteroid (162173) Ryugu. J Geophys Res. https://doi.org/10.1029/2020JE00651910.1002/essoar.10503201.2

Gundlach B, Blum J (2013) A new method to determine the grain size of planetary regolith. Icarus 223:479–492. https://doi.org/10.1016/j.icarus.2012.11.039

Hamm M, Hamilton VE, Goodrich CA (2023) Evidence for the presence of thin and heterogenous dust deposits on Ryugu's Boulders From Hayabusa2 MARA and Sample Data. Geophys Res Lett. https://doi.org/10.1029/2023GL104795

Hamm M, Grott M, Senshu H, Knollenberg J, de Wiljes J, Hamilton VE, Scholten F, Matz KD, Bates H, Maturilli A, Shimaki Y, Sakatani N, Neumann W, Okada T, Preusker F, Elgner S, Helbert J, Kührt E, HoTM, (2022) Tanaka S, Mid-infrared emissivity of partially dehydrated asteroid (162173) Ryugu shows strong signs of aqueous alteration. Nat Commun. https://doi.org/10.1038/s41467-022-28051-y

Hamm M, Pelivan I, Grott M, de Wiljes J (2020) Thermophysical modelling and parameter estimation of small Solar system bodies via data assimilation. MNRAS 496:2776–2785. https://doi.org/10.1093/mnras/staa1755

Hamm M, Senshu H, Grott M (2019) Latitudinal dependence of asteroid regolith formation by thermal fatigue. Icarus 319:308–311. https://doi.org/10.1016/j.icarus.2018.09.033

Hamm M, Grott M, Kührt E, Pelivan I, Knollenberg J (2018) A method to derive surface thermophysical properties of asteroid (162173) Ryugu (1999JU3) from in-situ surface brightness temperature measurements. Plan Space Sci 159:1–10. https://doi.org/10.1016/j.pss.2018.03.017

Hayne PO, Bandfield JL, Siegler MA, Vasavada AR, Ghent RR, Williams JP, Greenhagen BT, Aharonson O, Elder CM, Lucey PG, Paige DA (2017) Global regolith thermophysical properties of the Moon from the Diviner Lunar Radiometer Experiment. J Geophys Res (Planets) 122:2371–2400. https://doi.org/10.1002/2017JE005387

Kawakatsu Y, Kuramoto K, Usui T, Sugahara H, Ootake H, Yasumitsu R, Yoshikawa K, Mary S, Grebenstein M, Sawada H, Imada T, Shimada T, Ogawa K, Otsuki M, Baba M, Fujita K, Zacny K, van Dyne D, Satoh Y, Tokaji A (2023) Preliminary design of Martian Moons eXploration (MMX). Acta Astronaut 202:715–728. https://doi.org/10.1016/j.actaastro.2022.09.009

Kuehrt E, Giese B, Keller HU, Ksanfomality LV (1992) Interpretation of the KRFM infrared measurements of Phobos. Icarus 96:213–218. https://doi.org/10.1016/0019-1035(92)90075-I

Kuramoto K, Kawakatsu Y, Fujimoto M, Araya A, Barucci M-A, Genda H, Hirata N, Ikeda H, Imamura T, Helbert J, Kameda S, Kobayashi M, Kusano H, Lawrence DJ, Matsumoto K, Michel P, Miyamoto M, Morota T, Nakagawa H, Nakamura T, Ogawa K, Otake H, Ozaki M, Russel S, Sasaki S, Sawada H, Senshu H, Tachibana S, Terada N, Ulamec S et al (2022) Martian Moons Exploration MMX: sample return mission to phobos elucidating formation processes of habitable planets. Earth Planets Space 74:12–43. https://doi.org/10.1186/s40623-021-01545-7

Kessler E (2005) Proceedings of sensor 2005 12th international conference, Vol. I, Nürnberg, pp 73–78

Ksanfomality LV et al (1989) Spatial variations in thermal and albedo properties of the surface of Phobos. Nature 341:588–591. https://doi.org/10.1038/341588a0

Lagerros JSV (1996) Thermal physics of asteroids. I. Effects of shape, heat conduction and beaming. Astrono Astrophys 310:1011–1020

Lohrengel J, Todtenhaupt R, PTB-Mitteilungen 106:259–265 (1996)

Lucey PG, Greenhagen B, Donaldson HK, Bowles N, Flom A, Paige DA (2021) Christiansen feature map from the lunar reconnaissance orbiter diviner lunar radiometer experiment: improved corrections and derived mineralogy. J Geophys Res Planets 126(6):e06777. https://doi.org/10.1029/2020JE006777

Lunine JI, Neugebauer G, Jakosky BM (1982) Infrared observations of Phobos and Deimos from Viking. J Geophys Res 87:10297–10305. https://doi.org/10.1029/JB087iB12p10297

Michel P, Ulamec S, Böttger U, Grott M, Murdoch N, Vernazza P, Sunday C, Zhang Y, Valette R, Castellani R, Biele J, Tardivel S, Groussin O, Lorda L, Knollenberg J, Grundmann JT, Arrat D, Pont G, Mary S, Grebenstein M, Miyamoto H, Nakamura T, Wada K, Yoshikawa K, Kuramoto K (2022) The MMX rover: performing in situ surface investigations on Phobos. Earth Planets Space 74(1):2. https://doi.org/10.1186/s40623-021-01464-7

Molaro JL, Byrne S (2012) Rates of temperature change of airless landscapes and implications for thermal stress weathering. J Geophys Res. https://doi.org/10.1029/2012JE004138

Molaro JL, Byrne S, Le JL (2017) Thermally induced stresses in boulders on airless body surfaces, and implications for rock breakdown. Icarus 294(2017):247–261. https://doi.org/10.1016/j.icarus.2017.03.008
Mueller NT, Knollenberg J, Grott M, Kopp E, Walter I, Krause C, Hudson T, Spohn T, Smrekar S (2020) Calibration of the HP3 radiometer on InSight. Earth Space Sci 7(5):e01086. https://doi.org/10.1029/2020EA001086
Nakamura T, Ikeda H, Kouyama T, Nakagawa H, Kusano H, Senshu H, Kameda S, Matsumoto K, Gonzalez-Franquesa F, Ozaki N, Takeo Y, Baresi N, Oki Y, Lawrence DJ, Chabot NL, Peplowski PN, Barucci MA, Sawyer E, Yokota S, Terada N, Ulamec S, Michel P, Kobayashi M, Sasaki S, Hirata N, Wada K, Miyamoto H, Imamura T, Ogawa N, Ogawa K, Iwata T, Imada T, Otake H, Canalias E, Lorda L, Tardivel S, Mary S, Kunugi M, Mitsuhashi S, Doressoundiram A, Merlin F, Fornasier S, Reess JM, Bernardi P, Imai S, Ito Y, Ishida H, Kuramoto K, Kawakatsu Y (2021) Science operation plan of Phobos and Deimos from the MMX spacecraft. Earth Planets Space 73(1):227. https://doi.org/10.1186/s40623-021-01546-6
Ogawa K, Hamm M, Grott M, Sakatani N, Knollenberg J, Biele J (2019) Possibility of estimating particle size and porosity on Ryugu through MARA temperature measurements. Icarus 333:318–322. https://doi.org/10.1016/j.icarus.2019.06.014
Prokhorov AV, Mekhontsev SN, Hanssen LM (2003) Emissivity modeling of thermal radiation sources with concentric grooves. High Temperatures – High Pressures. 35/36, 199-207, 2003/2004. https://doi.org/10.1068/htjr093
Rüsch O, Marshal RM, Iqbal W, Pasckert JH, van der Bogert CH, Patzek M (2022) Catastrophic rupture of lunar rocks: implications for lunar rock size-frequency distributions. Icarus 387(115200):115200. https://doi.org/10.1016/j.icarus.2022.115200
Sapritsky VI, Khlevnoy BB, Khromchenko VB, Ogarev SA, Morozova SP, Lisiansky BEM, Samoylov ML, Shapoval VI, Sudarev KA (2003) Blackbody sources for the range 100 K to 3500 K for precision measurements in radiometry and radiation thermometry. https://doi.org/10.1063/1.1627196
Saunders P, White DR (2004) Interpolation errors for radiation thermometry. Metrologia 41:41–46. https://doi.org/10.1088/0026-1394/41/1/006
Sebastián E, Martínez G, Ramos M, Haenschke F, Ferrándiz R, Fernández Maite, Rodríguez Manfredi, JA (2020) Radiometric and angular calibration tests for the MEDA-TIRS radiometer onboard NASA's Mars 2020 Mission. Measurement. 164:107968. https://doi.org/10.1016/j.measurement.2020.107968
Smith NM, Edwards CS, Mommert M, Trilling DE, Glotch TD (2018) Mapping the thermal inertia of Phobos using MGS-TES observations and thermophysical modelling. In: 49th lunar and planetary science conference. The Woodlands, 19–23 Mar 2018
Spohn T, Seiferlin K, Hagermann A, Knollenberg J, Ball AJ, Banaszkiewicz M, Benkhoff J, Gadomski S, Gregorczyk W, Grygorczuk J, Hlond M, Kargl G, Kuehrt E, Kömle N, Krasowski J, Marczewski W, Zarnecki JC (2007) Mupus: a thermal and mechanical properties probe for the Rosetta Lander Philae. Space Sci Review 128:339–362. https://doi.org/10.1007/s11214-006-9081-2
Spohn T, Knollenberg J, Ball AJ, Banaszkiewicz M, Benkhoff J, Grott M, Grygorczuk J, Hüttig C, Hagermann A, Kargl G, Kaufmann E, Kömle N, Kuehrt E, Kossacki KJ, Marczewski W, Pelivan I, Schrödter R, Seiferlin K (2015) Thermal and mechanical properties of the near-surface layers of comet 67P/Churyumov-Gerasimenko. Science 349:6247. https://doi.org/10.1126/science.aab0464
Spohn T, Grott M, Smrekar SE, Knollenberg J, Hudson TL, Krause C, Müller N, Jänchen J, Börner A, Wippermann T, Krömer O, Lichtenheldt R, Wisniewski L, Grygorczuk J, Fittock M, Rheershemius S, Spröwitz T, Kopp E, Walter I, Plesa AC, Breuer D, Morgan P, Banerdt WB (2018) The heat flow and physical properties package (HP^{3}) for the insight mission. Space Sci Rev 214(5):96. https://doi.org/10.1007/s11214-018-0531-4
Ulamec S, Michel P, Grott M, Böttger U, Schröder S, Hübers HW, Cho Y, Rull F, Murdoch N, Vernazza P, Prieto-Ballesteros O, Biele J, Tardivel S, Arrat D, Hagelschuer T, Knollenberg J, Vivet D, Sunday C, Jorda L, Groussin O, Robin C, Miyamoto H (2023) Science objectives of the MMX rover. Acta Astronaut 210:5–101. https://doi.org/10.1016/j.actaastro.2023.05.012
Wolfe WL (1998) Introduction to Radiometry, SPIE Optical Engineering Press, Tutorial Texts in Optical Engineering, Volume TT29, Series Editor O'Shea DC, Bellingham, Washington, USA

Publisher's Note

Springer Nature remains neutral with regard to jurisdictional claims in published maps and institutional affiliations.